Head and Neck Pathology (2018) 12:302–320
https://doi.org/10.1007/s12105-018-0901-y

SPECIAL ISSUE: EAR

Cross Sectional Imaging of the Ear and Temporal Bone

Amy F. Juliano[1,2]

Received: 22 December 2017 / Accepted: 24 February 2018 / Published online: 1 August 2018

Abstract
CT and MR imaging are essential cross-sectional imaging modalities for assessment of temporal bone anatomy and pathology. The choice of CT versus MR depends on the structures and the disease processes that require assessment, delineation, and characterization. A thorough knowledge of the two imaging modalities' capabilities and of temporal bone anatomy greatly facilitates imaging interpretation of pathologic conditions.

Keywords Temporal bone · CT · MRI · Anatomy

Imaging Modalities

Imaging evaluation of the ear and temporal bone is primarily accomplished by computed tomography (CT) or magnetic resonance imaging (MRI). Each modality has its strengths and limitations. The patient's presenting symptoms and suspected diagnoses help guide the choice of modality.

CT offers better spatial resolution compared to MRI [1]. CT allows excellent delineation of calcifications, cortical bone, air, and fat. In the temporal bone region, therefore, CT is useful for assessing the margin and patency of the external auditory canal (EAC); thickness of the tympanic membrane, as it is bordered on either side by air, and whether there may be myringosclerosis, perforation, or retraction; margins, aeration, and opacities of the middle ear; and bony and calcified structures such as the ossicles, mastoid septations, otic capsule, morphology and margins of the cochlea and semicircular canals, vestibular aqueduct, and facial nerve canal.

MRI, on the other hand, offers much better, more specific, and more distinctive soft tissue characterization than CT [1]. On CT, if two soft tissue structures are similar in density (e.g. normal muscle and an adjacent sarcoma), they can be difficult to distinguish or demarcate from each other. But since MRI is not dependent on material density, but rather on spin properties of material at the subatomic particle level, they can behave quite differently within a magnetic field and produce quite different signal on various MR imaging sequences, allowing much better visual distinction. In the temporal bone region, MRI is useful for assessing for a mass in the internal auditory canal (IAC); abnormal cranial nerve caliber or enhancement; the fluid-filled spaces of the labyrinthine structures; for characterizing masses in the middle ear, for example to distinguish a cholesteatoma from an encephelocele; and for assessing marrow, for example in the setting of skull base osteomyelitis.

Temporal Bone CT

CT of the temporal bone must be performed at high-resolution and small field of view with thin imaging slices (0.5 mm), in order to be able to visualize the small, fine structures of the temporal bone to maximal detail. Images presented in an algorithm that highlights bone detail are most useful for assessment. Intravenous contrast is almost never necessary for the indications. In recent years, three-dimensional (3D) multiplanar reformatted/3D volume-rendered CT images have become available to help demonstrate anatomy and pathology of the temporal bone, with better appreciation of the morphology, orientation, and inter-relationships of the intricate and minute temporal bone structures in 3D space [2].

The temporal bone consists of five osseous components: squamous, mastoid, petrous, tympanic, and styloid. Important structures that are imaging landmarks are described in the following sections and illustrated on representative CT images in the axial and coronal planes (Figs. 1, 10) [3].

✉ Amy F. Juliano
amy_juliano@meei.harvard.edu

[1] Massachusetts Eye and Ear Infirmary, Boston, MA, USA

[2] Harvard Medical School, Boston, MA, USA

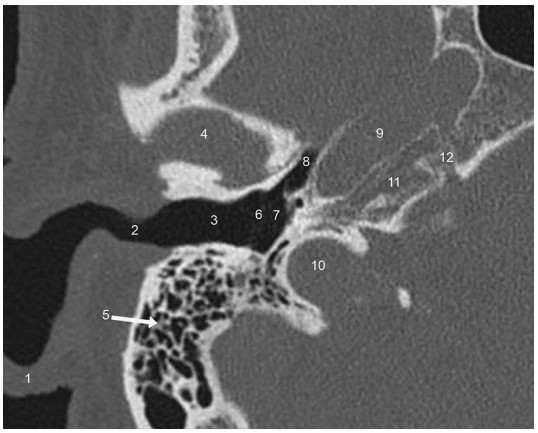

Fig. 1 CT, axial plane, at the level of the external auditory canal (EAC). Axial CT image in bone algorithm shows: *1* pinna, *2* fibrocartilaginous portion of EAC, *3* bony portion of EAC, *4* glenoid fossa, *5* mastoid portion of temporal bone, *6* tympanic membrane, *7* middle ear cavity, *8* eustachian tube opening, *9* petrous carotid canal, *10* jugular foramen, *11* petrous portion of temporal bone, *12* petroclival synchondrosis

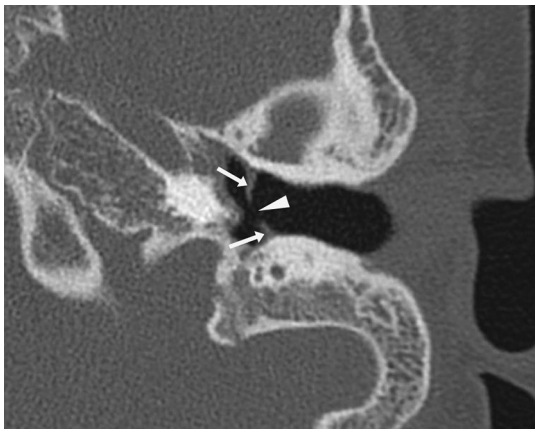

Fig. 2 Tympanic membrane perforation. Axial CT image shows a central defect in the tympanic membrane (arrowhead) compatible with a perforation. The remainder of the tympanic membrane is thickened (arrows)

External Auditory Canal

The external auditory canal (EAC) extends from the auricle to the tympanic membrane, the lateral portion fibrocartilaginous and the medial portion bony, formed by the tympanic portion of the temporal bone (Fig. 1). Anterior to the EAC is the glenoid fossa of the temporomandibular joint. Posterior to the EAC is the mastoid portion of the temporal bone. The tympanic membrane attaches to the tympanic annulus, and normally should only be faintly discernible on CT (Fig. 1). If it appears very well-defined, it is likely thickened, and increased density suggests myringosclerosis. A perforation appears as a focal defect (Fig. 2). A focal lobulated soft tissue opacity in the EAC (typically the inferior wall) with erosion of the adjacent bony wall may represent an EAC cholesteatoma (Fig. 3), [1, 4] although other possibilities such as carcinoma has to be excluded (Fig. 4). If an opacity causes focal obliteration of the EAC lumen and there is associated expansile widening and smooth scalloping of the surrounding walls but no frank bone erosion, keratosis obturans (Fig. 5) should be considered [5, 6].

Mastoid

The mastoid portion of the temporal bone is variably pneumatized. The mastoid air cells are divided by bony septations. In the central superior aspect is a larger cavity devoid of septations, termed the mastoid antrum. The mastoid antrum communicates with the epitympanum via a narrow waist termed the aditus ad antrum. If there is early-onset chronic or recurrent inflammation, the mastoid may be underpneumatized and sclerotic, with fewer mastoid air cells (Fig. 6) [7].

When mastoid air cells are opacified without associated bone changes, it is frequently due to an effusion; this may be inflammatory, obstructive related to eustachian tube obstruction or a nasopharyngeal mass (Fig. 7), or could be infectious. When the accumulated material is infectious and perhaps purulent, for example in the setting of infectious acute otitis media, there may be bony destruction involving the mastoid septations and/or overlying cortex associated with the mastoid opacities, termed coalescent mastoiditis (Fig. 8a, b) [8, 9]. If there is erosion of the lateral cortex, a subperiosteal abscess may develop in the postauricular region, which manifests clinically as a ballotable mass. If there is a bone defect at the mastoid tip medial to the insertion of the posterior belly of the digastric, an abscess may extend from the mastoid tip inferiorly deep to the sternocleidomastoid muscles, termed a Bezold abscess (Fig. 8c) [10, 11]. Infection may spread anteromedially to pneumatized petrous apex air cells as well, causing petrous apicitis, or to non-pneumatized petrous apex causing osteomyelitis (Fig. 9). Petrous apicitis occurring in association with sixth nerve palsy, deep retroorbital/facial pain in the trigeminal distribution, and otomastoiditis is termed Gradinego syndrome [12, 13]. Air cell opacity and bone erosion are best seen on CT (Fig. 9a),

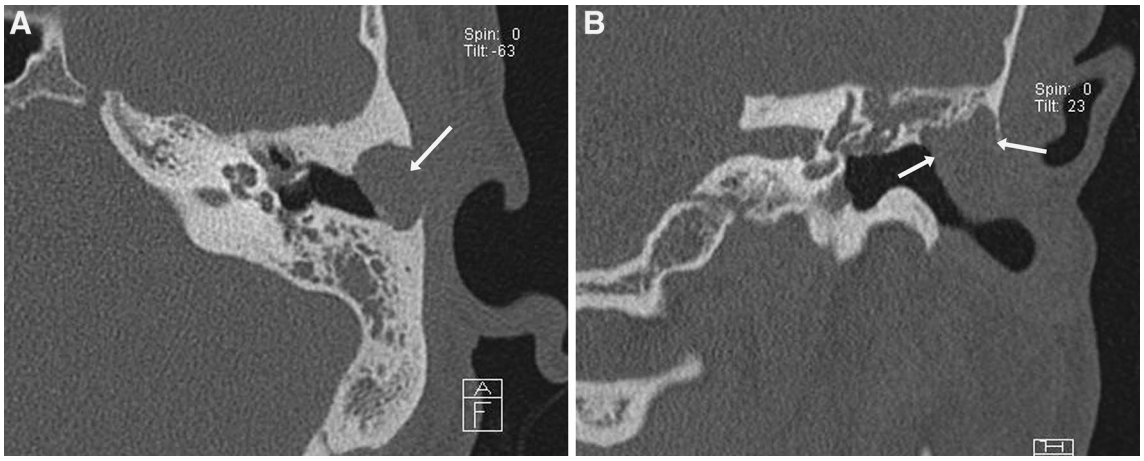

Fig. 3 EAC cholesteatoma. Axial (**a**) and coronal (**b**) CT images show a lobulated opacity causing pressure erosion of the adjacent bony margins of the EAC (arrows)

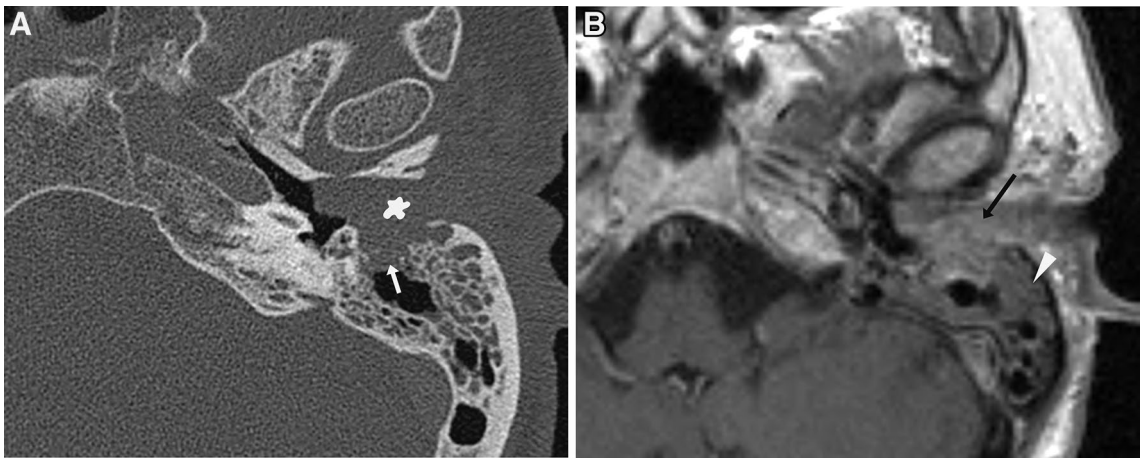

Fig. 4 Squamous cell carcinoma of the EAC. **a** Axial CT image through the left temporal bone shows a lobulated mass filling the EAC lumen (asterisk), invading into mastoid air cells (arrow), with erosion of the posterior margin of the bony EAC and mastoid septations. **b** Axial contrast-enhanced T1-weighted MR image on the same patient demonstrates intermediate enhancement of the soft tissue mass (black arrow), distinct from non-enhancing mastoid fluid which is hypointense on T1-weighted sequence (white arrowhead)

while abnormal enhancement of the dura, meninges, and cranial nerves, and any other intracranial complications are best assessed by MR imaging (Fig. 9b) [14].

It may be impossible to distinguish between coalescent mastoiditis and other entities on the basis of imaging alone. When there is mastoid opacification with bone erosion, other considerations include malignancy (most commonly squamous cell carcinoma), cholesteatoma, and, in children, Langerhans cell histiocytosis [15–17].

Middle Ear

The middle ear cavity is within the petrous portion of the temporal bone. Its lateral border is formed by the scutum and tympanic membrane (Fig. 10d). The scutum is a sharp bony projection pointed inferomedially from the mastoid temporal bone, its inferior tip being a point of attachment of the tympanic membrane. Its superior border is formed by the tegmen tympani, a thin bony plate that separates

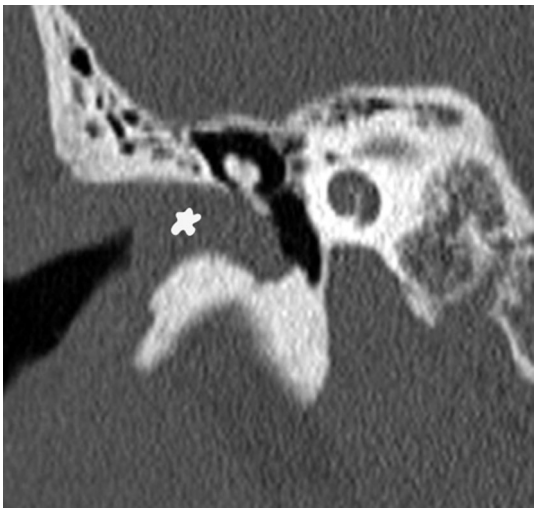

Fig. 5 Keratosis obturans. Coronal CT image through the right external auditory canal shows a smooth lobulated mass filling the canal lumen, with mild smooth expansile scalloping of the bony margins, but no frank erosion

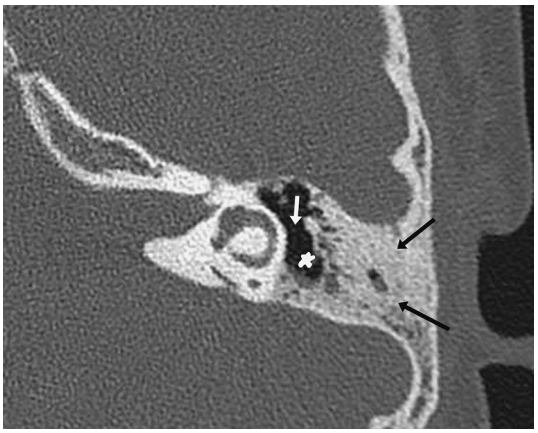

Fig. 6 Underpneumatized and sclerotic mastoid portion of the temporal bone. Axial CT image in an 8 year-old girl with underpneumatized and sclerotic mastoid (black arrows). The patient has a long-standing history of bilateral persistent and recurrent otitis media and multiple sets of myringotomy tubes. The mastoid antrum (asterisk) and aditus ad antrum (white arrow) can also be seen

the middle ear from the middle cranial fossa. If the tegmen shows abnormal downward bowing and contacts the malleus, there may be resultant limitation of ossicular chain movement and, therefore, conductive hearing loss. If a middle ear opacity abuts the tegmen and there is a bony defect in the tegmen, considerations would include an encephalocele and a cholesteatoma (Fig. 11). Fractures or defects at the tegmen can lead to a CSF fistula, manifest as CSF otorhinorrhea. High-resolution CT is extremely useful for assessment of tegmen defects. MR cisternography may be performed in conjunction to CT to detect secondary findings such as fluid/CSF in the middle ear or mastoid air cells and for a potential encephalocele [18].

Its medial border is formed by the otic capsule, the dense bone encasing the labyrinthine structures of the inner ear, with the inferior portion over the cochlea termed the cochlear promontory. The oval window, where the stapes attaches, is at roughly the midpoint, superior to the cochlear promontory. Superior to the oval window is the tympanic segment of the facial nerve, coursing from anterior to posterior. The developmental anomaly of oval window stenosis is frequently associated with a low-lying tympanic facial nerve (Fig. 12) [19, 20]. The inferior border of the middle ear is formed by the bony wall surrounding the internal jugular vein.

The anterior margin of the middle ear includes the anterior epitympanic recess, where a thin linear bony projection traversing its superior aspect may be seen on CT, termed the cog. More inferiorly is the opening to the eustachian tube. The posterior margin consists of two outwardly directed recesses separated by a bony protrusion called the pyramidal eminence; the recess lateral to it is the facial nerve recess, and the recess medial to it is the sinus tympani (Fig. 10). The stapedius muscle traverses the bony pyramidal eminence, extending through its tip into the middle ear and inserting onto the head of the stapes. Further medial to the sinus tympani closer to the medial wall is the round window niche, which borders the basal turn of the cochlea. Opacity in the normally aerated round window niche is often a non-specific finding. However, if there is a history of trauma, fluid in the round window niche may be due to a perilymphatic fistula, especially if this is seen in association with air in the vestibule [21].

The middle ear can be subdivided into the epitympanum (superior to the level of the tympanic membrane), mesotympanum (at the level of the tympanic membrane), and hypotympanum (inferior to the level of the tympanic membrane). The lateral portion of the epitympanum located between the scutum and the ossicles and inferior to the lateral malleal ligament is termed Prussak space (Fig. 10d). This is a favored location for a secondary acquired cholesteatoma, due to perforation or a retraction pocket of the pars flaccida and/or pars tensa, with accumulation of desquamated keratinizing squamous epithelium surrounded by a perimatrix of collagenous and elastic fibers, mixed inflammatory cells, granulation tissue, and neovascularity [1]. On CT, erosion of the scutum and ossicles by a focal rounded opacity in Prussak space is highly suggestive of an acquired cholesteatoma (Fig. 13)

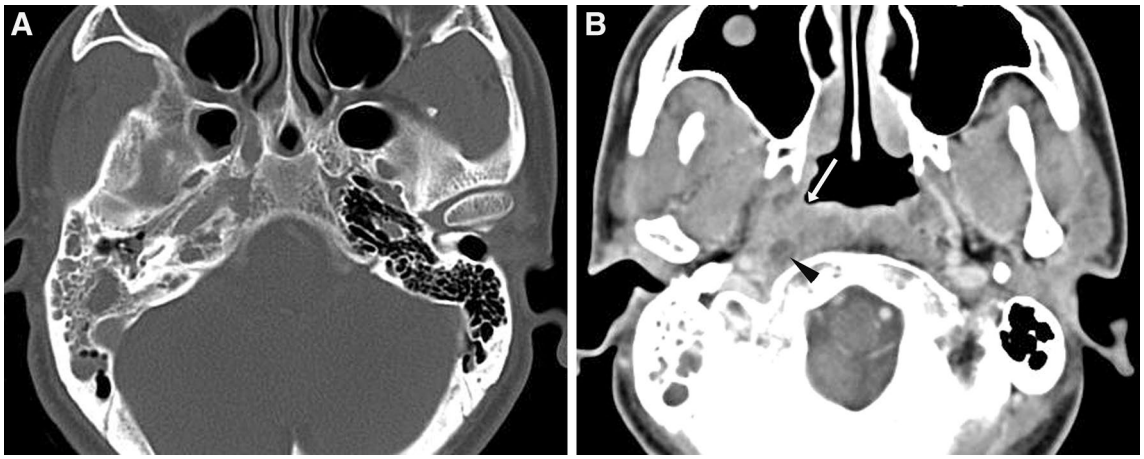

Fig. 7 Nasopharyngeal carcinoma. Contrast-enhanced CT in a 36 year old man. **a** Axial image in bone algorithm demonstrates opacities in the right middle ear and mastoid air cells without erosion of the bony septations. **b** Axial image in soft tissue algorithm demonstrates enhancing soft tissue filling the right fossa of Rosenmüller (white arrow) and an ipsilateral necrotic node of Rouvière (black arrowhead)

[22]. On the other hand, a congenital cholesteatoma of the middle ear tends to occur as a round mass in the anterior superior portion of an otherwise normal middle ear cavity just above the eustachian tube opening, and is thought to arise from embryonic epithelial rests [1, 23].

The ossicular chain is located almost entirely in the mesotympanum, consisting of the malleus (head, neck, anterior process, lateral process, and manubrium), incus (body, short process, long process, and lenticular process), and stapes (head/capitellum, anterior crus, posterior crus, and footplate) (Fig. 10). The manubrium of the malleus attaches to the tympanic membrane at the umbo. The head of the malleus articulates with the body of the incus at the incudomalleal joint, and the lenticular process of the incus articulates with the head of the stapes at the incudostapedial joint. The stapes footplate attaches to the oval window of the vestibule. With trauma, aside from soft tissue injury, one may see fractures through the mastoid and squamosal portions of the temporal bone, [24, 25] fractures through the otic capsule ("otic-capsule violating fracture") [26, 27] and facial nerve canal, [28, 29] and disruption to the ossicular chain [30]. The most common injury to the ossicular chain is incudostapedial joint separation (Fig. 14), due to the thin and fragile articulation between two axes of rotation, and/or simultaneous tetanic contractions of both the tensor tympani tendon (attaches to the malleus and can cause sudden incus retraction medially) and the stapedius tendon (attaches to the stapes and can cause stapes retraction posteriorly) [31]. The tensor tympani muscle arises from the eustachian tube and courses posteriorly to the middle ear, then takes a lateral turn sharply to attach to the neck of the malleus. The epitympanum continues posteriorly to the aditus ad antrum and mastoid antrum.

Inner Ear

The inner ear consists of the osseous labyrinth encased within the dense otic capsule. The structures of the osseous labyrinth include the cochlea, vestibule, and the three semicircular canals (superior, posterior, and lateral) (Fig. 10). These are well-delineated on CT by virtue of their sharp bony margins bordering on low fluid density within. The osseous labyrinth surrounds the membranous labyrinth, which includes the cochlear duct, utricle, saccule, semicircular ducts, endolymphatic duct, and endolymphatic sac; these structures of the membranous labyrinth cannot be visualized on CT. The fluid space within the membranous labyrinth is subdivided into three chambers: the scala media (containing endolymph), scala tympani (containing perilymph), and scala vestibuli (containing perilymph), also not distinguishable on CT.

The cochlea is spiral-shaped, comprising of a wide basal turn, middle turn, and a small apical turn, for a total of 2.5–2.75 turns. They are separated by bony interscalar septae, which can be seen on CT (Fig. 10b). In the center is the modiolus, a conical structure of spongy bone containing the spiral ganglion (Fig. 10b). The cochlear division of cranial nerve VIII courses along the anteroinferior portion of the internal auditory canal, through the cochlear fossette (canal for the cochlear nerve), and into the modiolus. From the modiolus, branches of the cochlear nerve are transmitted to

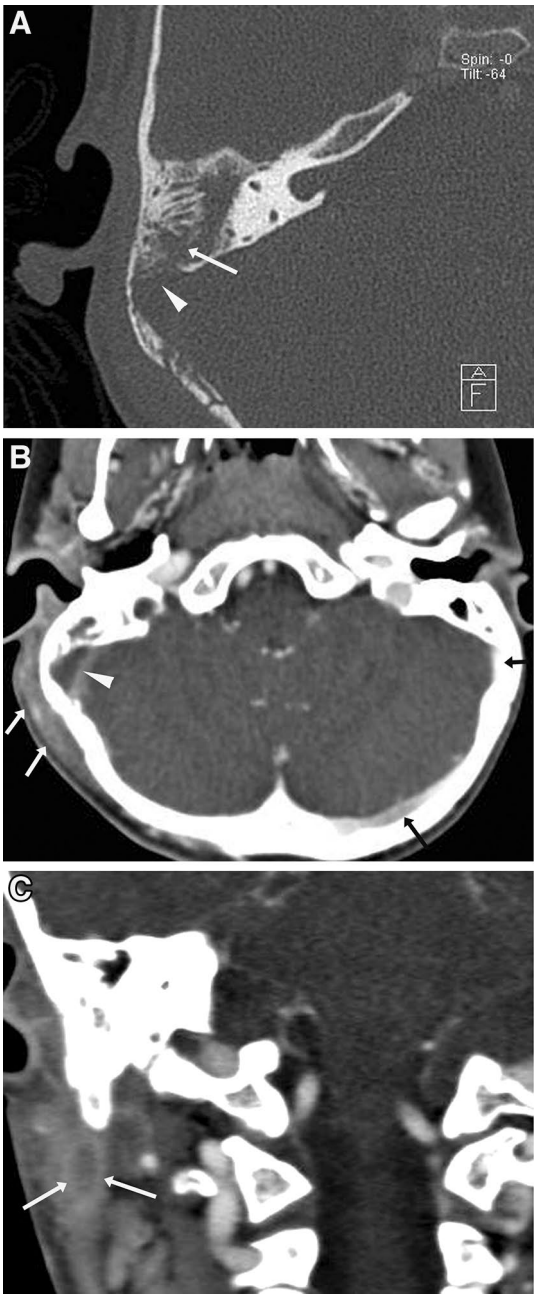

Fig. 8 Coalescent mastoiditis. CT on a 7 year-old boy with right acute otitis media complicated by coalescent mastoiditis. **a** Axial CT image of the right temporal bone in bone algorithm demonstrates opacification of the mastoid air cells and mastoid antrum, with dehiscence of some mastoid septations (arrow) and of the posterior cortex bordering on the sinodural angle (arrowhead). **b** Axial contrast-enhanced CT image in soft tissue algorithm shows soft tissue swelling lateral to the mastoid (arrows), and a filling defect in the sigmoid sinus (arrowhead) that may represent sigmoid sinus thrombosis or an epidural abscess compressing the adjacent sigmoid sinus. Notice normal contrast opacification of the contralateral transverse and sigmoid sinuses (black arrows). **c** Coronal image through the right mastoid region shows soft tissue swelling and a Bezold abscess (arrows) inferior to the mastoid tip

the organ of Corti, not visible on CT. Inner ear dysplasias are readily visualized on CT by virtue of the bony contour of the osseous labyrinth. Cochlear malformations ranging from complete labyrinthine aplasia, cochlear aplasia, to incomplete partition type I (IP-I) and incomplete partition type II (IP-II) (Fig. 15) are readily diagnosed on CT.

The lateral bony bulge formed by the lateral portion of the basal turn is the cochlear promontory (Fig. 10). The nerve of Jacobson (branch of cranial nerve IX) courses over the cochlear promontory. Therefore, a typical CT appearance of a glomus tympanicum (paraganglioma) is a round nodule in the middle ear abutting the cochlear promontory (Fig. 16), due to the tumor arising from paraganglia that are located along the nerve of Jacobson. Paragangliomas are avidly enhancing tumors, but that is difficult to appreciate on a CT, even if it is contrast-enhanced; soft tissue enhancement characteristics are better assessed by MRI.

The basal turn of the cochlea is contiguous superiorly and posteriorly with the vestibule, which in turn is connected to the superior, posterior, and lateral semicircular canals, oriented orthogonal to each other [32]. The superior and posterior semicircular canals share a common crus that opens into the vestibule, while the lateral semicircular canal has two separate openings into the vestibule. A so-called "third window" causing autophony, pseudo-conductive hearing loss, and Tullio phenomenon (sound-induced episodic vertigo and dysequilibrium) may be due to semicircular canal dehiscence (dehiscence of the bony covering over a semicircular canal); [33–36] this is well assessed by CT (Fig. 17) [37]. The superior semicircular canal is the most commonly involved (superior semicircular canal dehiscence, SSCD); some of these cases are due to close proximity of the superior semicircular canal to the groove for the superior petrosal sinus with a thin/dehiscent bony separation between the two structures. Rarely, a large cholesteatoma may erode the adjacent otic capsule and lead to dehiscence of the lateral semicircular canal.

As mentioned above, the membranous labyrinth contains fluid (perilymph and endolymph), which is hypodense on CT, surrounded by the very dense osseous labyrinth and otic capsule. If dense calcifications are seen within the membranous labyrinth, labyrinthitis ossificans is the likely diagnosis. Labyrinthitis ossificans is the late stage of labyrinthitis, where there is pathologic ossification of the normally fluid-filled chambers in the cochlea, vestibule, and semicircular canals (Fig. 18). The most common chamber affected is the scala tympani of the cochlea basal turn. Labyrinthitis occurs as a result of inner ear inflammation, which may be of post-traumatic (e.g. as seen with otic capsule violating fractures), autoimmune, or infectious etiologies [38]. The most extensive cases of labyrinthitis ossificans are seen in relation to

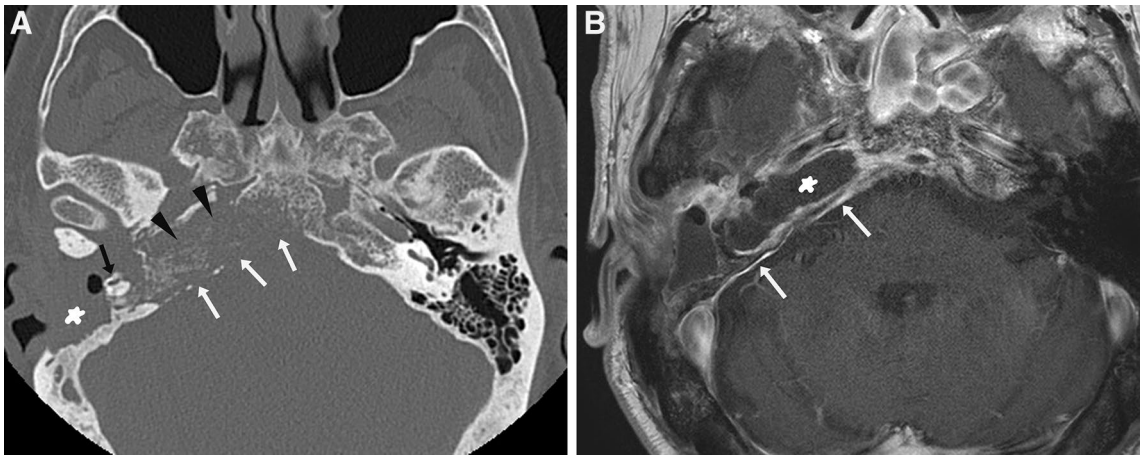

Fig. 9 Petrous apex osteomyelitis. **a** Axial CT image demonstrates complete opacification of the post-operative mastoid cavity (asterisk), erosion of the otic capsule (black arrow), and erosion of the right petrous apex and clivus. The posterior cortex (white arrows) and the margins of the right carotid canal (black arrowheads) are destroyed. **b** Axial contrast-enhanced T1-weighted MR image shows a fluid collection with peripheral enhancement in the petrous apex (asterisk) compatible with an abscess. Dural thickening and enhancement are much better appreciated by MRI than CT technique (arrows)

meningitis, often with bilateral involvement. Of note, CT is not as sensitive as MR for detection of early stage labyrinthitis when there is only proteinaceous or fibrous content in the fluid, which is not evident on CT but may be seen on MR heavily T2-weighted sequence images. But in the late stage of labyrinthitis ossificans, CT is more sensitive than MR for detecting ossification [39].

Otospongiosis (also termed otosclerosis) is an idiopathic osteodystrophy of the otic capsule, frequently bilateral and affecting women more than men, usually presenting with hearing loss in the 2nd to 4th decades of life [40]. The earliest area of the otic capsule to be affected is around the embryologic fissula ante fenestram, a thin fold of embryonic cartilage and connective tissue within a small cleft located just anterior to the oval window. Disease limited to this area results in conductive hearing loss, due to limitation of stapes footplate movement at the oval window, and is termed fenestral otospongiosis. On CT, this is appreciated as an area of hypodensity/lucency anterior to the oval window and vestibule (Fig. 19). The round window may also be involved, which may range from hypodensity at the bony edges of the round window to thickening of the round window membrane to abnormal calcification/otosclerotic foci filling and obliterating the round window niche [41]. With progressive disease involvement, the remainder of the otic capsule around the cochlea and adjacent to the lateral portion of the internal auditory canal is involved, leading to sensorineural hearing loss, and is termed retrofenestral or cochlear otospongiosis (Fig. 20) [42, 43].

The endolymphatic duct cannot be seen on CT, but the bony canal surrounding it, termed the vestibular aqueduct, can be well seen on CT. Large vestibular aqueduct (LVA) is the most common inner ear anomaly seen on imaging of patients with sensorineural hearing loss [44] and is usually associated with deficiency of the modiolus, with or without IP-II (Fig. 15) [45–47]. CT images reformatted in the Pöschl plane (45 degree sagittal oblique) allows optimal visualization of the vestibular aqueduct along its entire course, and is the plane best used to determine LVA [48]. Endolymphatic sac tumor is a benign but locally invasive papillary cystadenomatous tumor that may be seen in the setting of von Hippel Lindau disease or may be sporadic [49]. The tumor causes a characteristic appearance on CT consisting of expansile, moth-eaten, lytic destruction of the retrolabyrinthine temporal bone including the margins of the vestibular aqueduct (Fig. 21a), with a thin peripheral rim of calcification that represents the expanded cortex of the petrous bone. Intratumoral spicules are often seen. MRI is complementary, showing areas of intrinsic T1 hyperintense signal due to the presence of blood products, cholesterol clefts, and proteinaceous cysts. The tumor usually demonstrates

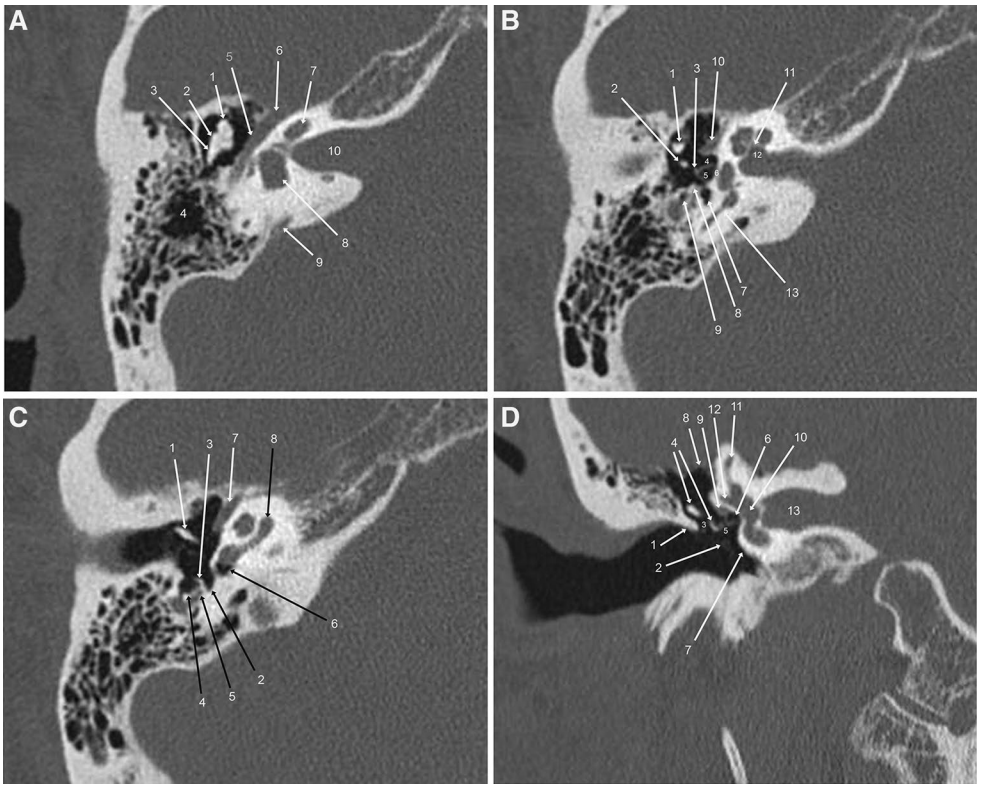

Fig. 10 CT images of the middle ear. **a** Axial plane, at the level of the mid epitympanum: *1* head of malleus, *2* body of incus, *3* short process of incus, *4* mastoid antrum, *5* tympanic segment of facial nerve, *6* geniculate ganglion, *7* cochlea, *8* vestibule, *9* vestibular aqueduct, *10* internal auditory canal. **b** Axial plane, at the level of the lower epitympanum: *1* neck of malleus, *2* long process of incus, *3* capitellum of stapes, *4* anterior crus of stapes, *5* posterior crus of stapes, *6* oval window, *7* sinus tympani, *8* pyramidal eminence, *9* facial nerve recess, *10* tensor tympani, *11* cochlear modiolus, *12* cochlear fossette, *13* posterior semicircular canal. **c** Axial plane, at the level of the mesotympanum: *1* manubrium of malleus, *2* sinus tympani, *3* pyramidal eminence, *4* facial nerve recess, *5* stapedius muscle, *6* round window niche, *7* tensor tympani, *8* cochlea basal turn. **d** Coronal plane, at the level of the oval window: *1* scutum, *2* tympanic membrane, *3* Prussak space, *4* incus, *5* incudostapedial joint, *6* oval window, *7* cochlear promontory, *8* tegmen tympani, *9* tympanic segment of facial nerve, *10* vestibule, *11* superior semicircular canal, *12* lateral semicircular canal, *13* internal auditory canal

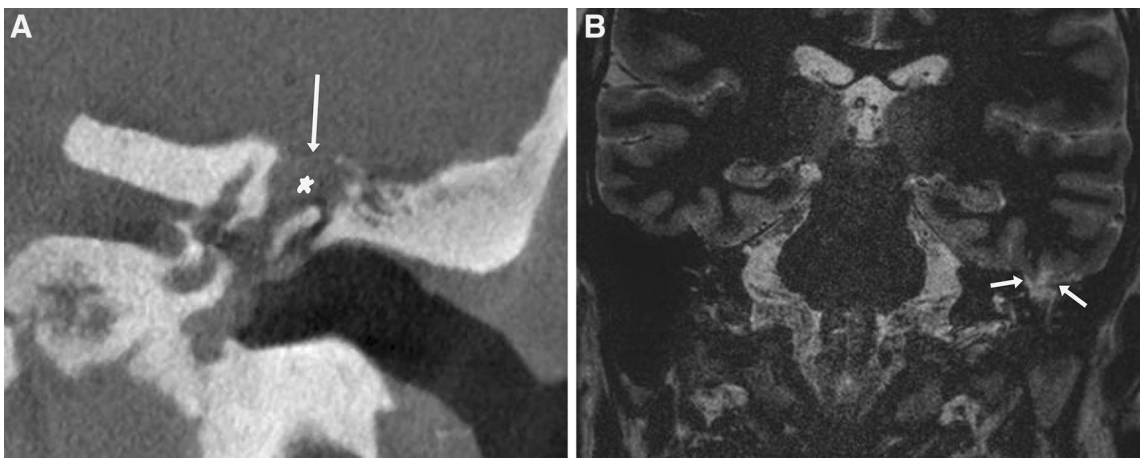

Fig. 11 Middle ear meningoencephalocele. **a** Coronal CT image through the left temporal bone shows a wide defect in the tegmen tympani (arrow). Opacity in the middle ear abutting the defect (asterisk) is non-specific, but a cholesteatoma and/or a meningoencephalocele are possible. **b** Coronal inversion recovery MR image shows herniation of brain and fluid through the tegmen defect (arrows), confirming a meningoencephalocele

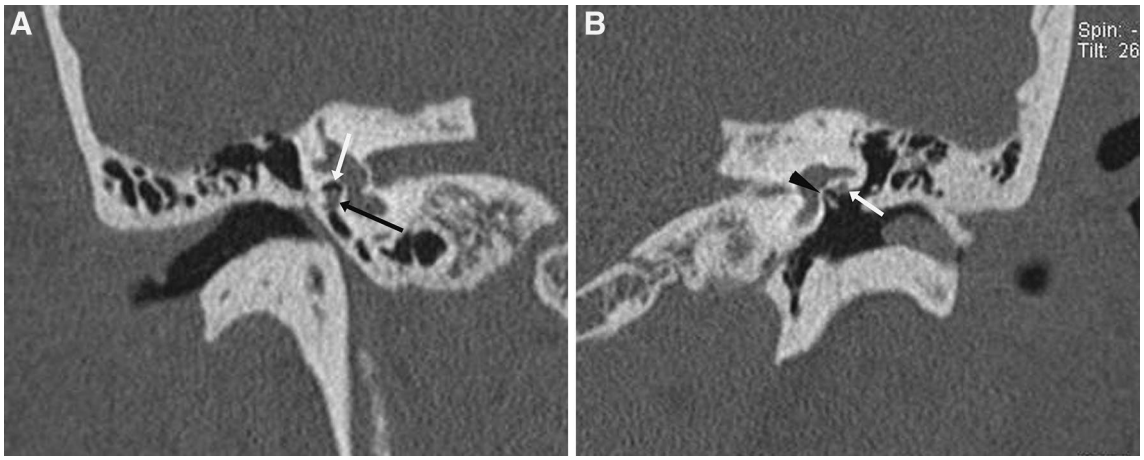

Fig. 12 Oval window stenosis. **a** Coronal CT image through the right temporal bone shows a stenotic and malformed oval window without a stapes (white arrow), and a low-lying tympanic nerve at/below the level of the stenotic oval window (black arrow). **b** Coronal CT image of the same patient through the normal left temporal bone. Note the presence of a stapes extending to the oval window (black arrowhead), and normal location of the tympanic facial nerve superior to the oval window (white arrow)

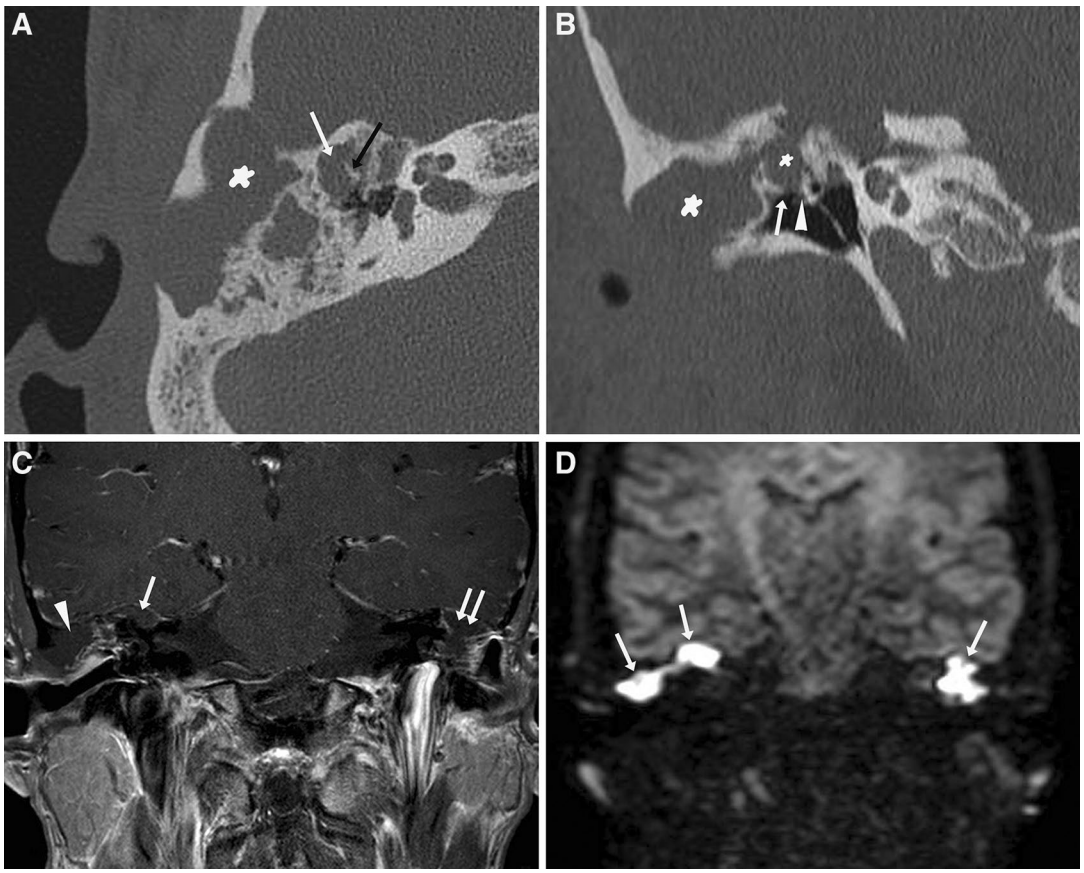

Fig. 13 Acquired cholesteatoma. **a** Axial CT image of the right temporal bone shows lobulated opacity in the middle ear (white arrow) and mastoid (asterisk). The head of the malleus and the incus have been eroded, and only the manubrium of the malleus remains (black arrow). **b** Coronal CT image shows erosion of the scutum (arrow) and ossicles (arrowhead) by the cholesteatoma (asterisks). Note absence of pars flaccida (between the arrow and the arrowhead), which is either retracted or perforated. **c** Coronal post-contrast T1-weighted image shows non-enhancement of the middle ear (arrow) and mastoid (arrowhead) masses, compatible with although not unique to cholesteatoma. Note that there is cholesteatoma on the left side as well (double arrows). **d** Coronal DWI shows the lesions demonstrating restricted diffusion, manifest as high signal intensity, diagnostic of cholesteatomas (arrows)

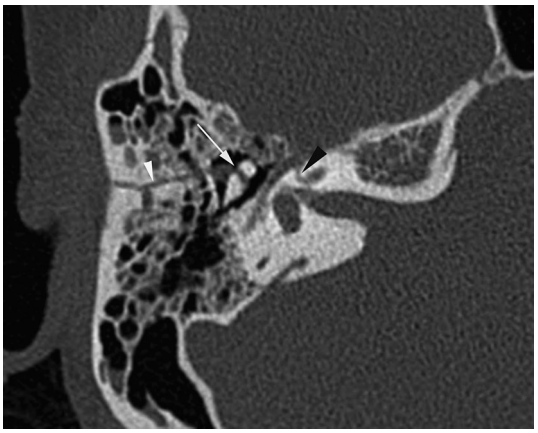

Fig. 14 Incudostapedial separation. Axial CT image shows abnormally widened space between the head of the malleus and the body of the incus (arrow) consistent with incudostapedial separation. Notice the presence of an otic-capsule-sparing (longitudinal) fracture (white arrowhead) as well as an otic-capsule-violating (transverse) fracture (black arrowhead) through the course of the facial nerve and the cochlea

heterogeneous enhancement (Fig. 21b). If catheter angiography is performed, the tumor demonstrates high vascularity, with blood supply from the ascending pharyngeal and stylomastoid arteries [50].

The cochlear aqueduct is located more caudally, and extends from the basal turn of the cochlea just anterior to the round window, to the subarachnoid space adjacent to the jugular foramen pars nervosa. It connects perilymph to the subarachnoid space.

Internal Auditory Canal

The internal auditory canal (IAC) is located between the porus acousticus medially and the fundus laterally (Fig. 10b). The facial nerve courses along the anterosuperior compartment of the IAC, then passes into the facial nerve canal in the temporal bone. The cochlear nerve courses along the anteroinferior compartment of the IAC, then through the cochlear fossette into the modiolus. The superior and inferior vestibular nerves course through the posterior half of the IAC [51]. It is difficult to appreciate soft tissue masses within the IAC on a CT. However, if the IAC is dilated and smoothly scalloped with a focally expansile appearance, an underlying mass should be suspected, most commonly a vestibular schwannoma. A meningioma tends to be centered at the cerebellopontine angle cistern (CPA) rather than the IAC, and does not cause expansion of the porus acousticus or IAC, although the surrounding bone might be involved with a mixed permeative/sclerotic/hyperostotic appearance (Fig. 22).

Facial Nerve

The facial nerve cannot be visualized on CT, but its intratemporal course and caliber can be inferred from the bony canal surrounding it [52]. The intratemporal segments as defined

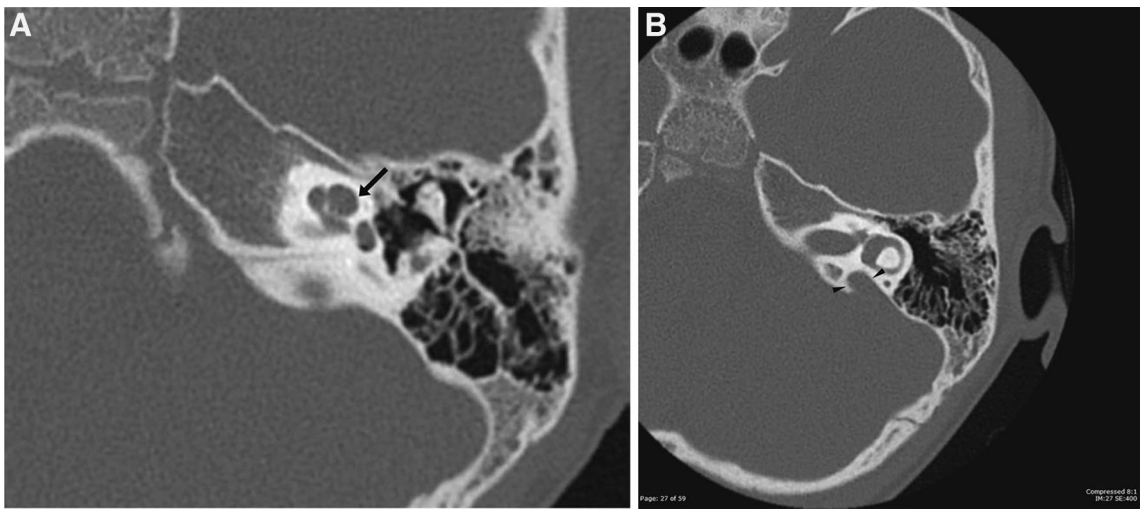

Fig. 15 Incomplete partition type II (IP-II) and large vestibular aqueduct (LVA). 3 year-old boy with left sensorineural hearing loss. Axial CT images of the left temporal bone in bone algorithm. **a** There is deficient interscalar septum between the middle and apical turns of the cochlea, giving a plump appearance to the mid-to-upper portion of the cochlea (black arrow). The modiolus is deficient (not shown on this image). **b** There is associated enlargement of the vestibular aqueduct (black arrowheads)

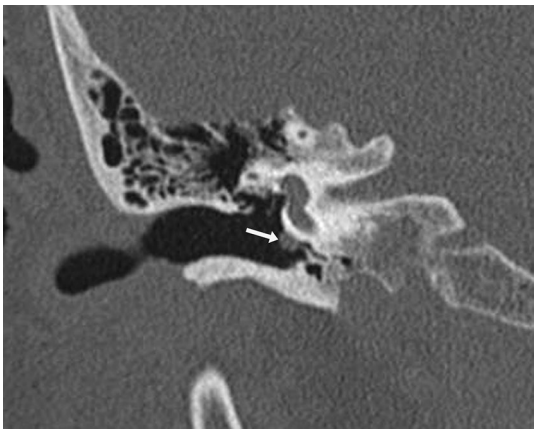

Fig. 16 Glomus tympanicum paraganglioma. Coronal CT image through the right temporal bone shows a round nodule in the middle ear against the cochlear promontory (arrow), characteristic of a glomus tympanicum in shape and location

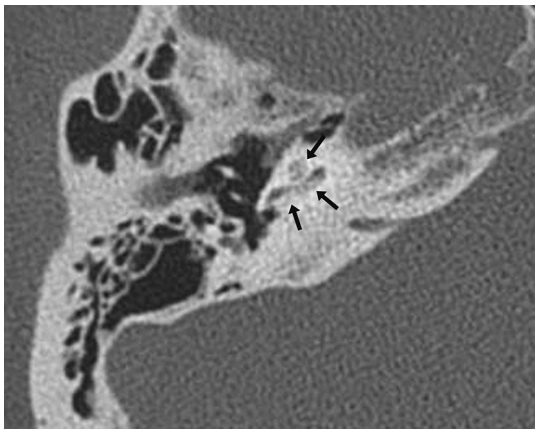

Fig. 18 Labyrinthitis ossificans. Axial CT image in bone algorithm demonstrates abnormal calcifications within the cochlea (arrows), compatible with labyrinthitis ossificans

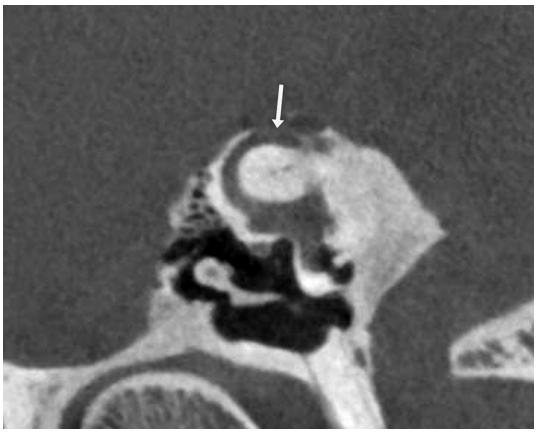

Fig. 17 Superior semicircular canal dehiscence. Sagittal oblique (Pöschl) view of the superior semicircular canal on CT demonstrates loss of normal bony covering over the superior semicircular canal (arrow)

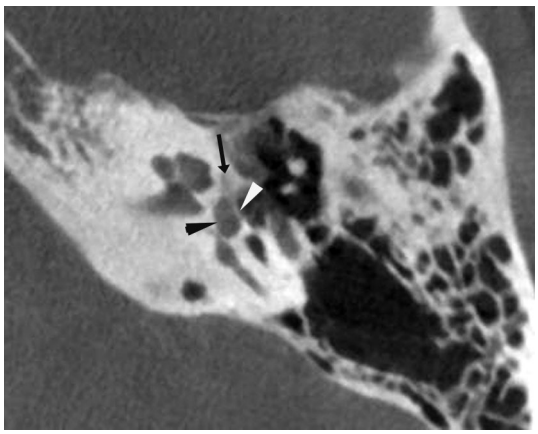

Fig. 19 Fenestral otospongiosis. Axial CT image demonstrates an area of relative hypodensity in the region of the embryologic fissula ante fenestram (black arrow), anterior to the vestibule (black arrowhead) and the stapes footplate (white arrowhead). This appearance is diagnostic of fenestral otospongiosis. There is no involvement of the remainder of the otic capsule

by location are: labyrinthine (through the petrous portion of the temporal bone), geniculate (where the geniculate ganglion is located, also termed the first genu), tympanic (through the medial aspect of the middle ear superior to the oval window) (Fig. 10a), and mastoid (inferiorly through the mastoid portion of the temporal bone to exit the skull base at the stylomastoid foramen). The greater superficial petrosal nerve branches off of the geniculate ganglion to course anteriorly. The nerve to the stapedius branches off

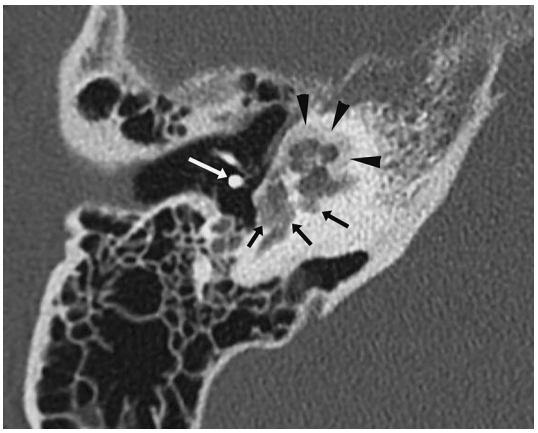

Fig. 20 Retrofenestral otospongiosis. Axial CT image shows hypodensity around the cochlea circumferentially (black arrowheads), and extensively around the vestibule and adjacent to the internal auditory canal (black arrows), compatible with retrofenestral otospongiosis. Note the patient has a stapes prosthesis (white arrow), placed in the past for fenestral otospongiosis to bypass the abnormal bone at the stapes footplate (not shown)

at the proximal mastoid segment at the level of the pyramidal eminence. The chorda tympani branches off of the mastoid segment further caudally, coursing superolaterally and anteriorly toward the middle ear. The bony channel through which the chorda tympani traverses is well seen on CT.

Normally, fat should be seen at the stylomastoid foramen, surrounding the exiting facial nerve. If the fat is obliterated, then pathology such as perineural spread of tumor should be considered (Fig. 23) [53, 54]. If the facial nerve canal is widened, in addition to perineural spread of tumor, a facial nerve schwannoma should be considered, and an MRI should be performed to assess for an expansile enhancing lesion along the entire course of the nerve (Fig. 24). When there is focal expansile appearance at the geniculate ganglion, additional considerations include a meningocele, a venous malformation (commonly but incorrectly referred to as "hemangioma"), [55] and an intraosseous meningioma. On CT, one may be able to appreciate small foci of bony spicules in a geniculate region venous malformation (Fig. 25a). Intraosseous meningioma tends to cause denser, more extensive, sclerotic, and expansile bony changes. Both show enhancement on MRI (Fig. 25b). An MRI is definitive for characterizing meningocele, appearing as a well-circumscribed, non-enhancing, rounded area of CSF signal intensity.

Temporal Bone MR

Bony anatomy and structures surrounded by air are best evaluated by CT, but MR is preferred for soft tissue assessment. High-resolution and small field of view imaging protocol must be employed for detailed assessment.

Important sequences include a heavily T2-weighted sequence with imaging slice thickness of 1 mm. This sequence renders fluid extremely bright, while all other structures are dark (Fig. 26). This allows structures or lesions residing within fluid-filled spaces to be assessed easily for size and contour, e.g. a vestibular schwannoma or meningioma (surrounded by CSF within the IAC or CPA), or an intralabyrinthine schwannoma within the

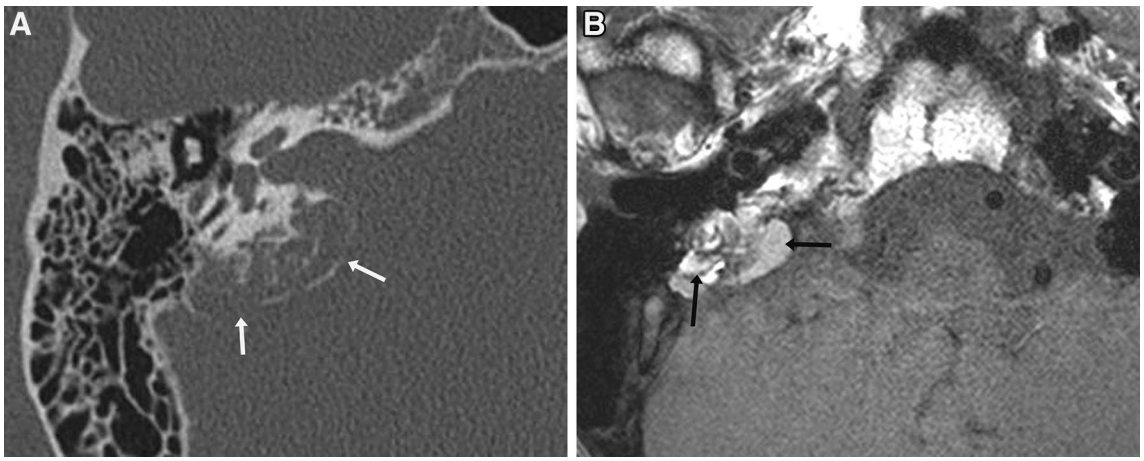

Fig. 21 Endolymphatic sac tumor. **a** Axial CT image shows an expansile, moth-eaten, lytic lesion in the retrolabyrinthine temporal bone, in the region of the vestibular aqueduct (white arrows). The vestibular aqueduct is involved in the area of eroded bone and can no longer be discerned. **b** Axial non contrast-enhanced T1-weighted MR image in the same patient demonstrates areas of intrinsic T1 hyperintense signal within the lesion (arrows), characteristic of an endolymphatic sac tumor

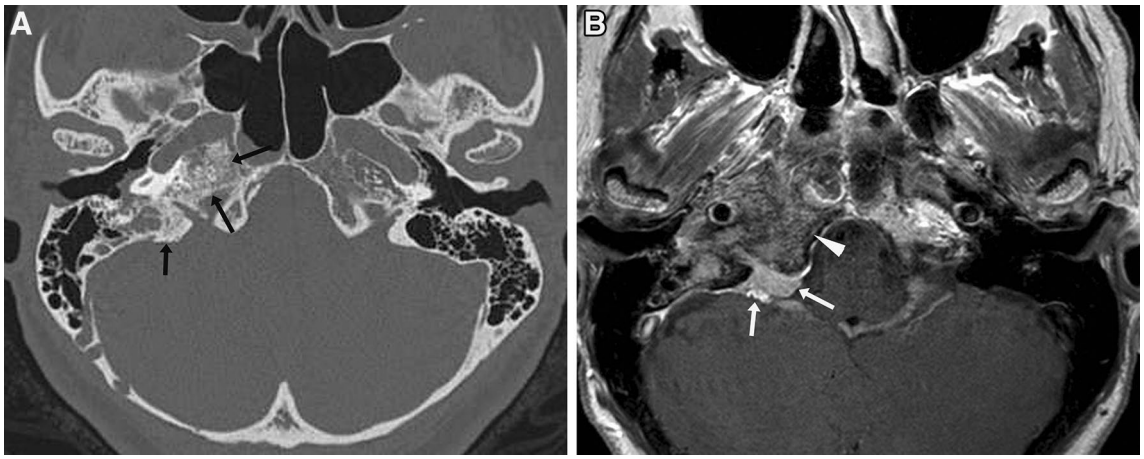

Fig. 22 Cerebellopontine angle cistern/jugular foramen meningioma. **a** Axial CT image in bone algorithm shows a mixed permeative/sclerotic/hyperostotic appearance of the petrous temporal bone where it abuts the meningioma (black arrows). **b** Axial post-contrast T1-weighted MR image shows the enhancing meningioma (white arrows). The adjacent marrow signal is decreased (arrowhead), due to replacement of normal marrow fat by the heterogeneous permeative/sclerotic/hyperostotic bone

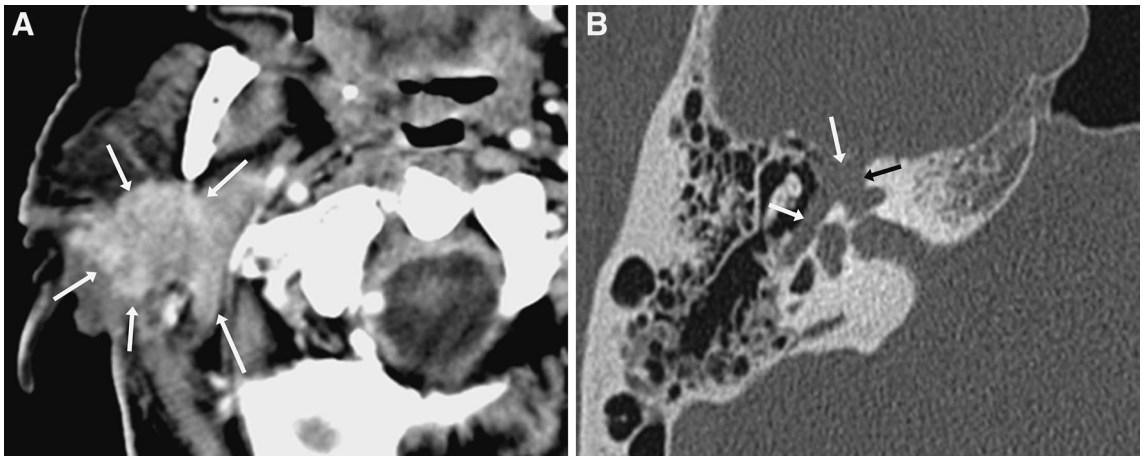

Fig. 23 Perineural spread of tumor. **a** Axial CT image in soft tissue algorithm shows an irregularly marginated enhancing mass in the right parotid gland infiltrating toward the skull base toward the stylomastoid foramen (arrows), extending along the facial nerve. **b** Axial CT image in bone algorithm shows diffuse widening of the facial nerve canal (arrows), secondary to thickening of the facial nerve within the canal from perineural tumor spread

cochlea or vestibule (outlined by fluid in the membranous labyrinth). It allows assessment of fluid content, which for example may be decreased in signal or obliterated in labyrinthitis ossificans. It also allows for delineation of the contour of the osseous labyrinth, such that inner ear dysplasia (e.g. incomplete partition types I and II, semicircular canal dysplasia) may be detected.

On the heavily T2-weighted sequence, cranial nerves VII and VIII coursing through the IAC can be seen as dark linear lines surrounded by bright fluid on axial images (Fig. 26), and as dark dots surrounded by bright fluid on sagittal oblique images oriented perpendicular to the long axis of the IAC (Fig. 27) [51]. The latter is useful for diagnosing cochlear nerve aplasia or hypoplasia, where only three dots

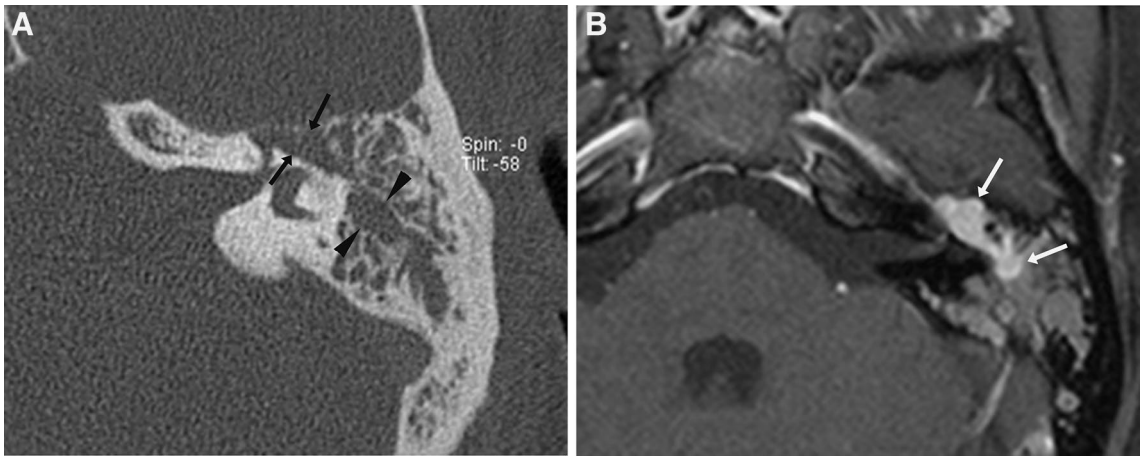

Fig. 24 Facial nerve schwannoma. **a** Axial CT image in bone algorithm shows smooth expansile appearance of the tympanic facial nerve canal in a non-contiguous fashion (between arrows and between arrowheads). **b** Axial contrast-enhanced T1-weighted image shows the tubular expansile enhancing schwannoma (arrows) causing the bone expansion

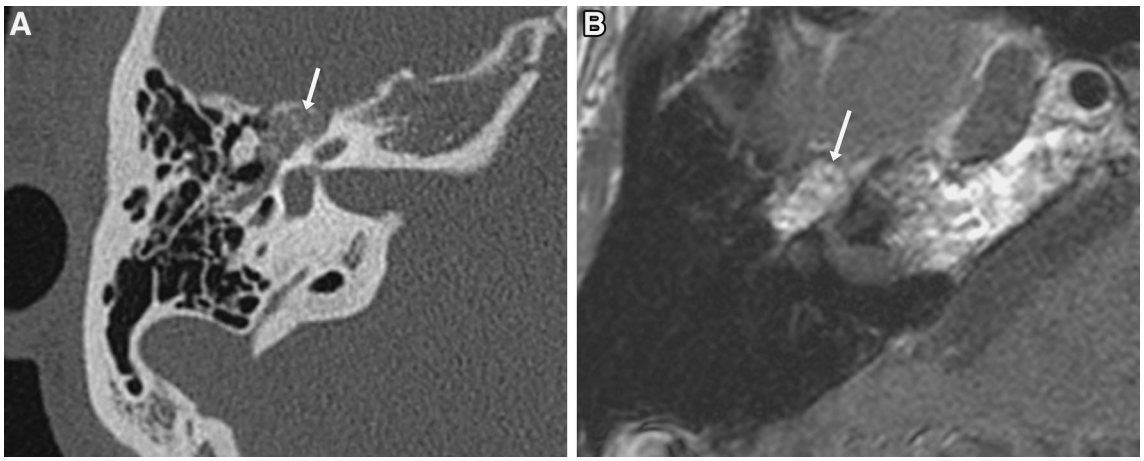

Fig. 25 Geniculate venous malformation. **a** Axial CT image in bone algorithm shows an expansile lobulated mass centered at the geniculate ganglion, with internal foci of bony spicules (arrow). **b** Axial contrast-enhanced T1-weighted image shows the avid enhancement of this lesion, compatible with a venous malformation

(representing the facial nerve, and superior and inferior vestibular nerves) would be seen, rather than the usual 4.

Pre- and post-contrast enhanced T1-weighted sequences with imaging slice thickness of 2 mm are also essential, as it helps to detect enhancing abnormalities (e.g. facial or vestibular neuritis and tumors, [56] and dural metastasis or leptomeningeal carcinomatosis extending into the internal auditory canal) (Fig. 28), as well as determine enhancement characteristics and pattern in order to narrow the differential diagnosis. Examples include: (1) in the middle ear, a non-enhancing cholesteatoma versus an avidly enhancing glomus tympanicum; (2) in the IAC and CPA, enhancement of a lobulated mass favoring a vestibular schwannoma versus enhancement of a hemispheric mass with serrated enhancing edges and enhancing dural tail favoring a meningioma; (3) in the middle ear and at the jugular foramen, a "salt-and-pepper" pattern of avid enhancement with small internal flow voids favoring a paraganglioma (Fig. 29) rather than a schwannoma or meningioma [3].

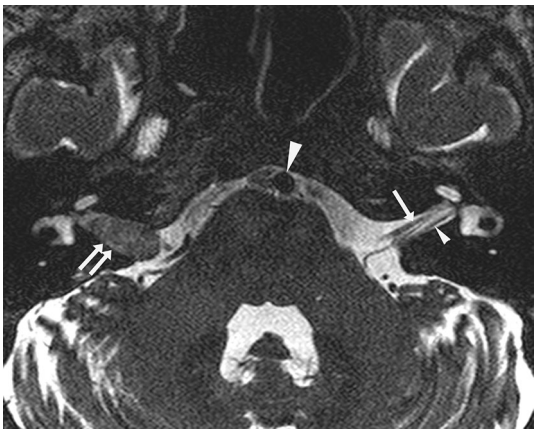

Fig. 26 Heavily T2-weighted MR sequence in the axial plane, showing a right internal auditory canal (IAC) mass. Axial heavily T2-weighted high-resolution image through the internal auditory canals. Fluid is bright, while all other structures are dark. This allows superior visualization of structures surrounded by fluid, such as the cochlear nerve (white arrow), inferior vestibular nerve (small white arrowhead), and vessels coursing through CSF-filled cisternal spaces such as the basilar artery (large white arrowhead). The fluid-filled components of the labyrinth are well outlined. A mass occupying the right internal auditory canal is well seen (double arrows), with location and morphology compatible with a vestibular schwannoma

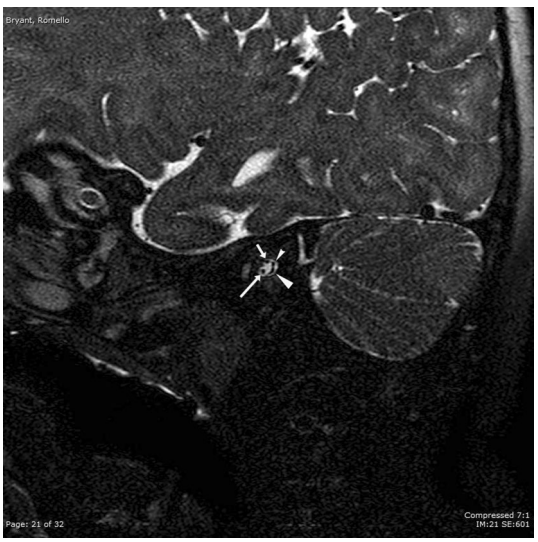

Fig. 27 Heavily T2-weighted MR sequence in the sagittal oblique plane through the IAC. Heavily T2-weighted MR image in the sagittal oblique plane through the IAC shows the facial nerve (short arrow), cochlear nerve (long arrow), superior vestibular nerve (small arrowhead), and inferior vestibular nerve (large arrowhead). Cochlear nerve hypoplasia or aplasia can be diagnosed from this MR sequence if the cochlear nerve appears small or is absent

Special sequences are sometimes employed for specific diagnoses. A coronal diffusion weighted imaging (DWI) sequence is performed through the middle ear and mastoid for diagnosis of a cholesteatoma, which exhibits reduced diffusivity, appearing as a hyperintense focus on a DWI sequence (Fig. 30) [1, 57, 58]. Non-echo-planar imaging (non-EPI) turbo spin-echo-based DWI technique can achieve thinner sections (2 mm) with less susceptibility artifact at the bone-air interface, and is preferred to EPI DWI technique [3, 59]. Axial diffusion weighted imaging is useful for distinguishing an epidermoid from an arachnoid cyst in the cerebellopontine angle cistern; the former exhibits reduced diffusion, [1] while the latter has normal diffusivity and follows CSF signal. Coronal and sagittal inversion recovery sequences allow superior contrast of gray and white matter against bone and CSF, and can help define the position and contour of the brain and CSF relative to the bony floor of the middle cranial fossa and the temporal bone, aiding in detection of meningoencephaloceles in the middle ear or mastoid. (Fig. 31). A fat-suppressed T1-weighted sequence is useful for diagnosis of a lipoma in the IAC or CPA. Fat-suppressed post-contrast T1-weighted sequences are used in post-operative patients in assessing for recurrence of vestibular schwannoma, as there is often fat-packing in the CPA placed during surgery that may be confused for enhancing tumor in the absence of fat signal suppression [60, 61].

MR imaging is especially useful in characterizing a round, expansile lesion in the petrous apex. If the internal contents follow simple or proteinaceous fluid on all sequences, it is likely a mucocele. Reduced diffusivity without associated enhancement is pathognomonic for a cholesteatoma (epidermoid). Intrinsic T1 hyperintensity is diagnostic of a cholesterol granuloma [62–66].

Summary

In conclusion, CT and MR imaging are essential cross-sectional imaging modalities for assessment of temporal bone anatomy and pathology. The choice of CT versus MR depends on the structures and the disease processes that require assessment, delineation, and characterization. A thorough knowledge of the two imaging modalities' capabilities and of temporal bone anatomy greatly facilitates imaging interpretation of pathologic conditions.

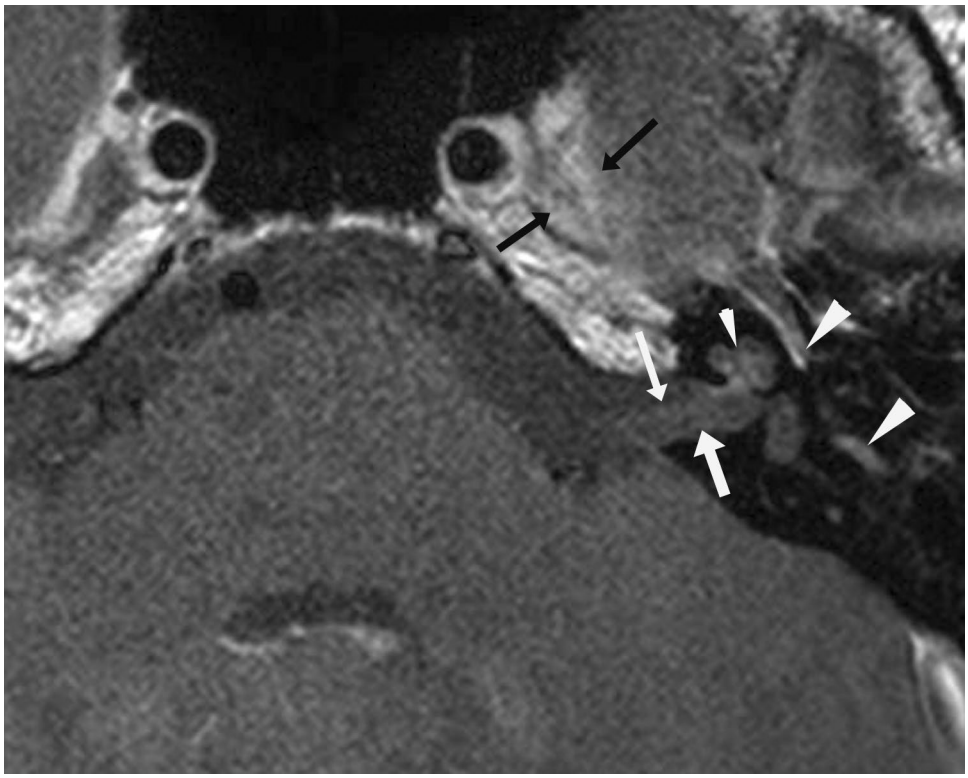

Fig. 28 Ramsey Hunt syndrome. A 43 year-old man with Ramsey Hunt syndrome. Axial contrast-enhanced T1-weighted image shows abnormal mild enhancement along the cochlear nerve (thin arrow) continuing into the cochlea (small arrowhead), and along the vestibular nerve (thick arrow) and facial nerve (large arrowheads). There is also enhancement in left Meckel cave (black arrows), due to involvement of the trigeminal nerve

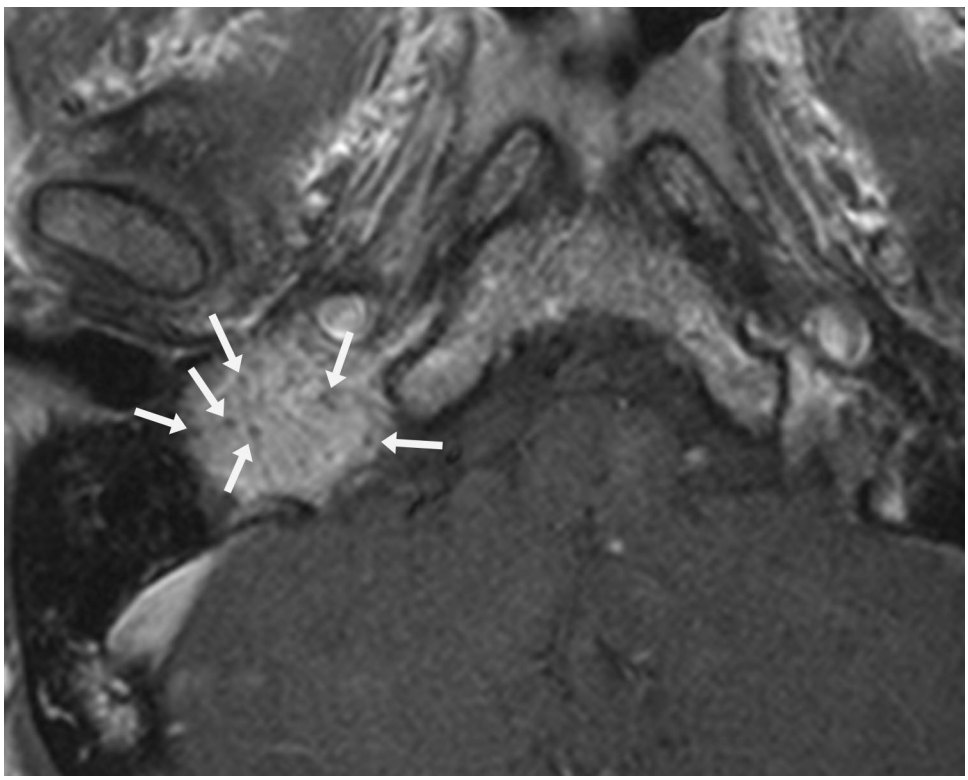

Fig. 29 Glomus jugulare paraganglioma on MRI. Axial contrast-enhanced T1-weighted image through the right skull base demonstrates an avidly enhancing mass with internal flow voids (arrows) centered at the jugular foramen, giving the lesion a "salt-and-pepper" appearance that is characteristic of a paraganglioma

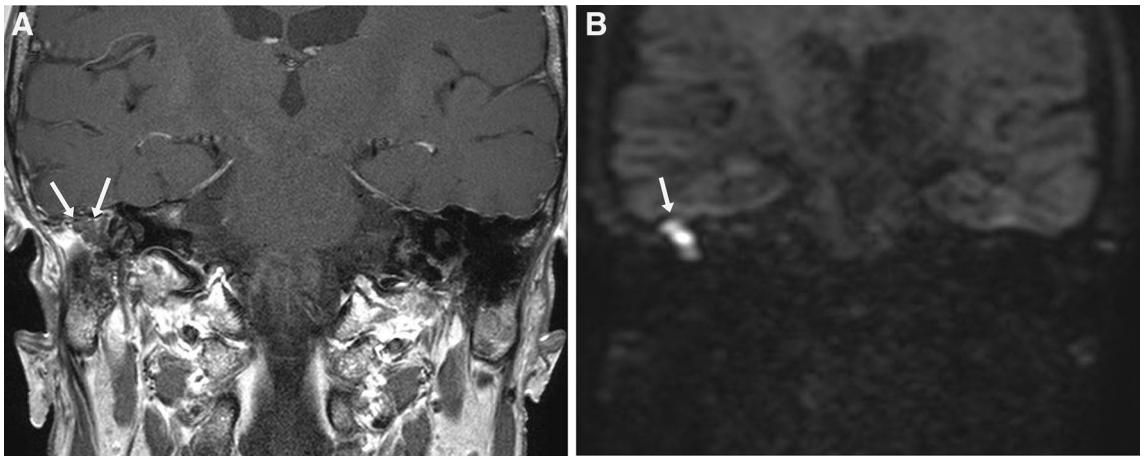

Fig. 30 Cholesteatoma on MRI. **a** Coronal contrast-enhanced T1-weighted image shows non-enhancing material in the lateral epitympanum and upper mastoid region on the right (arrows). **b** This material exhibits reduced diffusivity on coronal DWI sequence, manifest as high signal intensity (arrow), diagnostic of a cholesteatoma

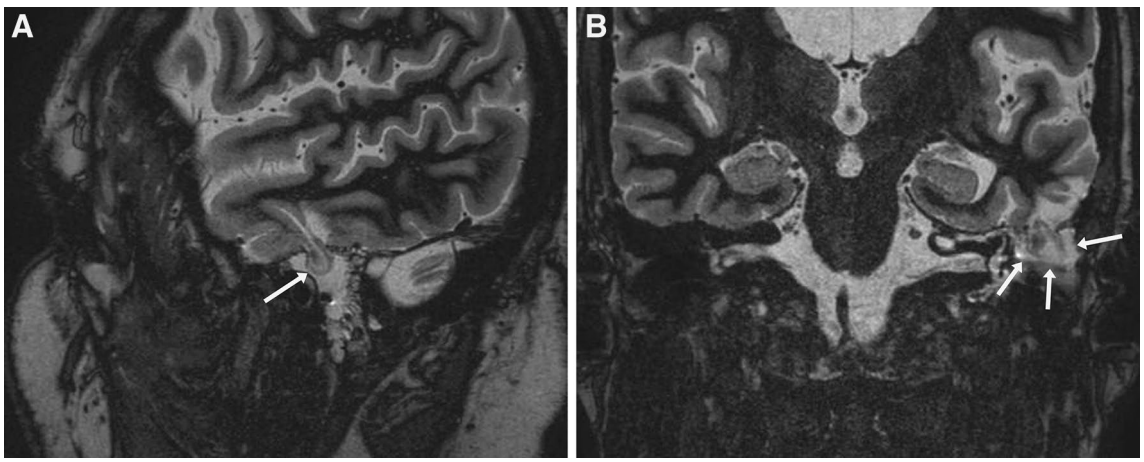

Fig. 31 Encephalocele. Sagittal (**a**) and coronal (**b**) inversion recovery sequences show inferior herniation of gliotic brain and CSF through a wide tegmen defect (arrows)

References

1. Barath K, Huber AM, Stampfli P, Varga Z, Kollias S. Neuroradiology of cholesteatomas. AJNR Am J Neuroradiol. 2011;32:221–9.
2. Fatterpekar GM, Doshi AH, Dugar M, Delman BN, Naidich TP, Som PM. Role of 3D CT in the evaluation of the temporal bone. Radiographics 2006;26(Suppl 1):S117–32.
3. Juliano AF, Ginat DT, Moonis G. Imaging review of the temporal bone: part I. Anatomy and inflammatory and neoplastic processes. Radiology 2013;269:17–33.
4. Dubach P, Hausler R. External auditory canal cholesteatoma: reassessment of and amendments to its categorization, pathogenesis, and treatment in 34 patients. Otol Neurotol. 2008;29:941–8.
5. Piepergerdes MC, Kramer BM, Behnke EE. Keratosis obturans and external auditory canal cholesteatoma. Laryngoscope 1980;90:383–91.
6. Tran LP, Grundfast KM, Selesnick SH. Benign lesions of the external auditory canal. Otolaryngol Clin North Am. 1996;29:807–25.
7. Virapongse C, Sarwar M, Bhimani S, Sasaki C, Shapiro R. Computed tomography of temporal bone pneumatization: 2. Petrosquamosal suture and septum. AJNR Am J Neuroradiol. 1985;6:561–8.
8. Levine HR, Ha KY, O'Rourke B, Owens FD, Doughty KE, Opatowsky MJ. A pictorial review of complications of acute coalescent mastoiditis. In Baylor University Medical Center Proceedings 2012 (Vol. 25, No 4, pp. 372–373). Taylor & Francis.
9. Zevallos JP, Vrabec JT, Williamson RA, et al. Advanced pediatric mastoiditis with and without intracranial complications. Laryngoscope 2009;119:1610–5.
10. Anand AG, Amedee RC. Bezold's abscess: a unique complication of otitis media. J La State Med Soc. 2009;161:25–9.
11. Marioni G, de Filippis C, Tregnaghi A, Marchese-Ragona R, Staffieri A. Bezold's abscess in children: case report and review of the literature. Int J Pediatr Otorhinolaryngol. 2001;61:173–7.
12. Vitale M, Amrit M, Arora R, Lata J. Gradenigo's syndrome: a common infection with uncommon consequences. Am J Emerg Med. 2017;35:1388e1–e2.

13. Gadre AK, Chole RA. The changing face of petrous apicitis-a 40-year experience. Laryngoscope 2018;128:195–201.
14. Vazquez E, Castellote A, Piqueras J, et al. Imaging of complications of acute mastoiditis in children. Radiographics 2003;23:359–72.
15. Hu XD, Wu TT, Zhou SH. Squamous cell carcinoma of the middle ear: report of three cases. Int J Clin Exp Med. 2015;8:2979–84.
16. Majumder A, Wick CC, Collins R, Booth TN, Isaacson B, Kutz JW. Pediatric langerhans cell histiocytosis of the lateral skull base. Int J Pediatr Otorhinolaryngol. 2017;99:135–40.
17. Abdel-Aziz M, Rashed M, Khalifa B, Talaat A, Nassar A. Eosinophilic granuloma of the temporal bone in children. J Craniofac Surg. 2014;25:1076–8.
18. Shetty PG, Shroff MM, Sahani DV, Kirtane MV. Evaluation of high-resolution CT and MR cisternography in the diagnosis of cerebrospinal fluid fistula. AJNR Am J Neuroradiol. 1998;19:633–9.
19. Zeifer B, Sabini P, Sonne J. Congenital absence of the oval window: radiologic diagnosis and associated anomalies. AJNR Am J Neuroradiol. 2000;21:322–7.
20. Booth TN, Vezina LG, Karcher G, Dubovsky EC. Imaging and clinical evaluation of isolated atresia of the oval window. AJNR Am J Neuroradiol. 2000;21:171–4.
21. Malis DJ, Magit AE, Pransky SM, Kearns DB, Seid AB. Air in the vestibule: computed tomography scan finding in traumatic perilymph fistula. Otolaryngol Head Neck Surg. 1998;119:689–90.
22. Gaurano JL, Joharjy IA. Middle ear cholesteatoma: characteristic CT findings in 64 patients. Ann Saudi Med. 2004;24:442–7.
23. El-Bitar MA, Choi SS, Emamian SA, Vezina LG. Congenital middle ear cholesteatoma: need for early recognition–role of computed tomography scan. Int J Pediatr Otorhinolaryngol. 2003;67:231–5.
24. Saraiya PV, Aygun N. Temporal bone fractures. Emerg Radiol. 2009;16:255–65.
25. Collins JM, Krishnamoorthy AK, Kubal WS, Johnson MH, Poon CS. Multidetector CT of temporal bone fractures. Semin Ultrasound CT MRI. 2012;33:418–31.
26. Ishman SL, Friedland DR. Temporal bone fractures: traditional classification and clinical relevance. Laryngoscope 2004;114:1734–41.
27. Dahiya R, Keller JD, Litofsky NS, Bankey PE, Bonassar LJ, Megerian CA. Temporal bone fractures: otic capsule sparing versus otic capsule violating clinical and radiographic considerations. J Trauma. 1999;47:1079–83.
28. Coker NJ. Management of traumatic injuries to the facial nerve. Otolaryngol Clin North Am. 1991;24:215–27.
29. Lambert PR, Brackmann DE. Facial paralysis in longitudinal temporal bone fractures: a review of 26 cases. Laryngoscope 1984;94:1022–6.
30. Meriot P, Veillon F, Garcia JF, et al. CT appearances of ossicular injuries. Radiographics 1997;17:1445–54.
31. Swartz JD, Zwillenberg S, Berger AS. Acquired disruptions of the incudostapedial articulation: diagnosis with CT. Radiology 1989;171:779–81.
32. Lemmerling M, Vanzieleghem B, Dhooge I, Van Cauwenberge P, Kunnen M. CT and MRI of the semicircular canals in the normal and diseased temporal bone. Eur Radiol. 2001;11:1210–9.
33. Yew A, Zarinkhou G, Spasic M, Trang A, Gopen Q, Yang I. Characteristics and management of superior semicircular canal dehiscence. J Neurol Surg B Skull Base. 2012;73:365–70.
34. Minor LB, Solomon D, Zinreich JS, Zee DS. Sound- and/or pressure-induced vertigo due to bone dehiscence of the superior semicircular canal. Arch Otolaryngol Head Neck Surg. 1998;124:249–58.
35. Minor LB. Clinical manifestations of superior semicircular canal dehiscence. Laryngoscope 2005;115:1717–27.
36. Carey JP, Minor LB, Nager GT. Dehiscence or thinning of bone overlying the superior semicircular canal in a temporal bone survey. Arch Otolaryngol Head Neck Surg. 2000;126:137–47.
37. Eibenberger K, Carey J, Ehtiati T, Trevino C, Dolberg J, Haslwanter T. A novel method of 3D image analysis of high-resolution cone beam CT and multi slice CT for the detection of semicircular canal dehiscence. Otol Neurotol. 2014;35:329–37.
38. Aralasmak A, Dincer E, Arslan G, Cevikol C, Karaali K. Post-traumatic labyrinthitis ossificans with perilymphatic fistulization. Diagn Interv Radiol. 2009;15:239–41.
39. Braun T, Dirr F, Berghaus A, et al. Prevalence of labyrinthine ossification in CT and MR imaging of patients with acute deafness to severe sensorineural hearing loss. Int J Audiol. 2013;52:495–9.
40. Purohit B, Hermans R, Op de Beeck K. Imaging in otosclerosis: a pictorial review. Insights Imaging. 2014;5:245–52.
41. Mansour S, Nicolas K, Ahmad HH. Round window otosclerosis: radiologic classification and clinical correlations. Otol Neurotol. 2011;32:384–92.
42. Lee TC, Aviv RI, Chen JM, Nedzelski JM, Fox AJ, Symons SP. CT grading of otosclerosis. AJNR Am J Neuroradiol. 2009;30:1435–9.
43. Valvassori GE. Imaging of otosclerosis. Otolaryngol Clin North Am. 1993;26:359–71.
44. Dewan K, Wippold FJ 2nd, Lieu JE. Enlarged vestibular aqueduct in pediatric sensorineural hearing loss. Otolaryngol Head Neck Surg. 2009;140:552–8.
45. Naganawa S, Ito T, Iwayama E, et al. MR imaging of the cochlear modiolus: area measurement in healthy subjects and in patients with a large endolymphatic duct and sac. Radiology 1999;213:819–23.
46. Reinshagen KL, Curtin HD, Quesnel AM, Juliano AF. Measurement for detection of incomplete partition Type II anomalies on MR imaging. AJNR Am J Neuroradiol. 2017;38:2003–7.
47. Berrettini S, Forli F, Bogazzi F, et al. Large vestibular aqueduct syndrome: audiological, radiological, clinical, and genetic features. Am J Otolaryngol. 2005;26:363–71.
48. Juliano AF, Ting EY, Mingkwansook V, Hamberg LM, Curtin HD. Vestibular aqueduct measurements in the 45 degrees Oblique (Poschl) plane. AJNR Am J Neuroradiol. 2016;37:1331–7.
49. Nevoux J, Nowak C, Vellin JF, et al. Management of endolymphatic sac tumors: sporadic cases and von Hippel-Lindau disease. Otol Neurotol. 2014;35:899–904.
50. Ayadi K, Mahfoudh KB, Khannous M, Mnif J. Endolymphatic sac tumor and von Hippel-Lindau disease: imaging features. AJR Am J Roentgenol. 2000;175:925–6.
51. Rubinstein D, Sandberg EJ, Cajade-Law AG. Anatomy of the facial and vestibulocochlear nerves in the internal auditory canal. AJNR Am J Neuroradiol. 1996;17:1099–105.
52. Tuccar E, Tekdemir I, Aslan A, Elhan A, Deda H. Radiological anatomy of the intratemporal course of facial nerve. Clin Anat. 2000;13:83–7.
53. Parker GD, Harnsberger HR. Clinical-radiologic issues in perineural tumor spread of malignant diseases of the extracranial head and neck. Radiographics 1991;11:383–99.
54. Nemzek WR, Hecht S, Gandour-Edwards R, Donald P, McKennan K. Perineural spread of head and neck tumors: how accurate is MR imaging? AJNR Am J Neuroradiol. 1998;19:701–6.
55. Benoit MM, North PE, McKenna MJ, Mihm MC, Johnson MM, Cunningham MJ. Facial nerve hemangiomas: vascular tumors or malformations? Otolaryngol Head Neck Surg. 2010;142:108–14.
56. Martin-Duverneuil N, Sola-Martinez MT, Miaux Y, et al. Contrast enhancement of the facial nerve on MRI: normal or pathological?. Neuroradiology 1997;39:207–12.
57. De Foer B, Vercruysse JP, Bernaerts A, et al. Detection of postoperative residual cholesteatoma with non-echo-planar

diffusion-weighted magnetic resonance imaging. Otol Neurotol. 2008;29:513–7.
58. Dremmen MH, Hofman PA, Hof JR, Stokroos RJ, Postma AA. The diagnostic accuracy of non-echo-planar diffusion-weighted imaging in the detection of residual and/or recurrent cholesteatoma of the temporal bone. AJNR Am J Neuroradiol. 2012;33:439–44.
59. Vercruysse JP, De Foer B, Pouillon M, Somers T, Casselman J, Offeciers E. The value of diffusion-weighted MR imaging in the diagnosis of primary acquired and residual cholesteatoma: a surgical verified study of 100 patients. Eur Radiol. 2006;16:1461–7.
60. Ginat DT, Martuza RL. Postoperative imaging of vestibular schwannomas. Neurosurg Focus. 2012;33:E18.
61. Carlson ML, Van Abel KM, Driscoll CL, et al. Magnetic resonance imaging surveillance following vestibular schwannoma resection. Laryngoscope 2012;122:378–88.
62. Razek AA, Huang BY. Lesions of the petrous apex: classification and findings at CT and MR imaging. Radiographics 2012;32:151–73.
63. Schmalfuss IM. Petrous apex. Neuroimaging Clin N Am. 2009;19:367–91.
64. Connor SE, Leung R, Natas S. Imaging of the petrous apex: a pictorial review. Br J Radiol. 2008;81:427–35.
65. Tringali S, Linthicum FH Jr. Cholesterol granuloma of the petrous apex. Otol Neurotol. 2010;31:1518–9.
66. Pisaneschi MJ, Langer B. Congenital cholesteatoma and cholesterol granuloma of the temporal bone: role of magnetic resonance imaging. Top Magn Reson Imaging. 2000;11:87–97.